



## REFLECT DELIVERABLE D2.2

### Report on gas solubility and degassing kinetic (type C)



#### *Summary:*

This report describes the activities performed within Task 1.2 “Report on gas solubility and degassing kinetic (type C)” until the end of month 40 of the REFLECT project. Two series of experiments have been carried out that assess the degassing process of type C geothermal fluids respectively in bulk and porous media. This has resulted in an improved understanding of the process and the associated physical phenomena by utilizing experimental equipment and data analysis tools specifically created for this task.


#### *Authors:*

Chris Boeije<sup>1</sup>, Cas Verweij<sup>1</sup>, Anushka Tripathi<sup>1</sup>, Wolfgang Weinzierl<sup>2</sup>, Pacelli Zitha<sup>1</sup> and Anne Pluymakers<sup>1</sup>

<sup>1</sup> Delft University of Technology, <sup>2</sup> GFZ German Research Centre for Geosciences



<b>Title:</b>	Report on gas solubility and degassing kinetic (type C)		
<b>Lead beneficiary:</b>	TUD		
<b>Other beneficiaries:</b>	GFZ		
<b>Due date:</b>	30 April 2023		
<b>Nature:</b>	Public		
<b>Diffusion:</b>	All partners, EC and general public		
<b>Status:</b>	Final		
<b>Document code:</b>	REFLECT_D2.2		
<b>DOI:</b>	<a href="https://doi.org/10.48440/gfz.4.8.2023.004">https://doi.org/10.48440/gfz.4.8.2023.004</a>		
<b>License information:</b>	CC-BY-4.0		
<b>Recommended citation:</b>	<i>Boeije, C.S., Verweij, C., Tripathi, A., Weinzierl, W., Zitha, P.L.J., Pluymakers, A.H.M.,</i> The H2020 REFLECT project: Deliverable 2.2 - Report on gas solubility and degassing kinetic (type C), <i>GFZ German Research Centre for Geosciences,</i> DOI: <a href="https://doi.org/10.48440/gfz.4.8.2023.004">https://doi.org/10.48440/gfz.4.8.2023.004</a>		
<b>Associated Data:</b>	Data associated with this publication are available from the following repository: <i>Boeije, C.S., et al.</i> REFLECT deliverable 2.2: Report on gas solubility and degassing kinetic (type C). <i>4TU.ResearchData</i> <a href="https://doi.org/10.4121/77e70250-9c14-413e-baaf-595580215cc6">https://doi.org/10.4121/77e70250-9c14-413e-baaf-595580215cc6</a>		
<b>Revision history</b>	Author	Delivery date	Summary of changes and comments
<b>Version 01</b>	CB	06.04.2023	Initial draft
<b>Version 02</b>	CB	26.04.2023	Addressed comments from WP partners

Approval status				
	Name	Function	Date	Signature
<b>Deliverable responsible</b>	Chris Boeije		26.04.2023	
<b>WP leader</b>	Anne Pluymakers			
<b>Reviewer</b>	Katrin Kieling	Project manager	25.04.2023	
<b>Project Coordinator</b>	Simona Regenspurg			

This document reflects only the author's view and the European Commission is not responsible for any use that may be made of the information it contains.

## TABLE OF CONTENTS

Table of contents.....	3
1 EXECUTIVE SUMMARY .....	4
2 Design of coreflood apparatus suitable for CT assisted experiments .....	5
3 Degassing kinetics of high salinity geothermal fluids .....	7
3.1 INTRODUCTION .....	7
3.2 MATERIALS AND METHODS .....	7
3.2.1 Experimental setup .....	8
3.2.2 Experimental procedure.....	9
3.2.3 Data analysis methods .....	9
3.2.4 Overview of experiments .....	10
3.2.5 Model description .....	10
3.3 RESULTS AND DISCUSSION.....	11
3.3.1 Comparison of experimental and modelled bubble points .....	11
3.3.2 Gaseous vs. supercritical bubbles .....	13
3.4 CONCLUSIONS AND RECOMMENDATIONS.....	15
4 reduction of effective permeability due to CO <sub>2</sub> degassing .....	16
4.1 INTRODUCTION .....	16
4.2 MATERIALS AND METHODS .....	17
4.2.1 Experimental setup .....	17
4.2.2 Experimental procedure.....	19
4.2.3 Data analysis.....	20
4.3 RESULTS AND DISCUSSION.....	22
4.3.1 Typical results.....	22
4.3.2 Effect of brine salinity .....	23
4.3.3 CT experiments.....	26
4.4 CONCLUSIONS AND RECOMMENDATIONS.....	31
5 CONCLUSION .....	32
6 List of publications .....	33
7 References.....	33

---

## 1 EXECUTIVE SUMMARY

Geothermal fluids often contain large quantities of dissolved gases, such as CO<sub>2</sub> and N<sub>2</sub>. Production of these fluids results in a pressure drop towards the extraction well. This disturbs the state of equilibrium of the geothermal water with its dissolved components, which can lead to the formation of free gas bubbles. The free gas can cause various problems such as corrosion of the facilities and increased levels of mineral scaling. The gas bubbles also take up space inside the pores of the reservoir rock, thereby limiting the ability for the water to flow. As this reduction occurs mainly near the extraction well it can reduce production of geothermal waters substantially.

The objective of this task (2.2) is to investigate the conditions under which free gas bubbles begin to form in a geothermal well or reservoir with a specific focus on high salinity fluids. To this end degassing experiments in bulk and porous media are performed to investigate the conditions under which bubbles form and their effect on the production process.

Bulk experiments were done by studying the degassing process inside a high-pressure visual cell. The objective of these experiments is to improve the understanding of the conditions under which free gas nucleates in geothermal reservoirs. The cell is filled with brine saturated with dissolved CO<sub>2</sub> at high pressure and temperature, which is subsequently depressurized to determine the bubble point pressure. Experiments were performed at high pressure (up to 200 bar) and temperature (up to 150 °C). A model based on the geochemical software PHREEQC was created for simulating the degassing behaviour at the same conditions as those used in the experiments. From these simulations, the theoretical bubble point pressures and temperatures were estimated along with the rate of gas exsolution during a depressurization process and then compared with the measured data.

To assess the impact of degassing on flow in porous media, a series of coreflood (i.e. flow through rock cores) experiments was carried out using a Berea sandstone core. Here the aim was to determine the conditions under which degassing starts and quantitatively assess any associated permeability decrease. Using a higher salinity brine as the aqueous phase causes the degassing process to start at a higher pressure due to reduced CO<sub>2</sub> solubility. The extent to which the effective permeability is reduced by the formation of free gas is only very slightly affected by salinity. CT visualization of the degassing process showed that at low CO<sub>2</sub> concentrations a fairly stable free gas front forms that moves upstream into the core as the back pressure is lowered. This is not the case at higher concentrations, where the effects of gravity override are more pronounced. For all experiments performed here, the effective permeability of the medium is reduced by approximately a factor ten in the regions where degassing takes place.

## 2 DESIGN OF COREFLOOD APPARATUS SUITABLE FOR CT ASSISTED EXPERIMENTS

Some of the experiments performed within this project focus on the visualization of free gas bubbles forming inside rock cores during coreflood experiments. The aim is to determine to which extent the formation of free gas bubbles affect flow inside the rock. This chapter provides a description of experimental apparatus used for these tests. CT imaging of the rock core is employed to visualize the flow inside the rock.

A 40 cm long and 4 cm diameter rock core is housed inside a PEEK core holder, which is placed horizontally inside the CT scanner. PEEK is used due to its minimized effect on the CT scans compared to other materials, that is, the scanning artefacts introduced by the core holder's material are minimal. The pressure along the length of the core is monitored during the experiments to assess the effect that the free gas bubbles have on the flow inside the rock core using various pressure transducers. Pressure within the core itself is measured at five locations and additional transducers are installed up- and downstream of the core. A schematic overview of the setup used in these experiments outlining its most important components is given in Figure 1. These most relevant parts are numbered in the figure and are also listed in Table 1.

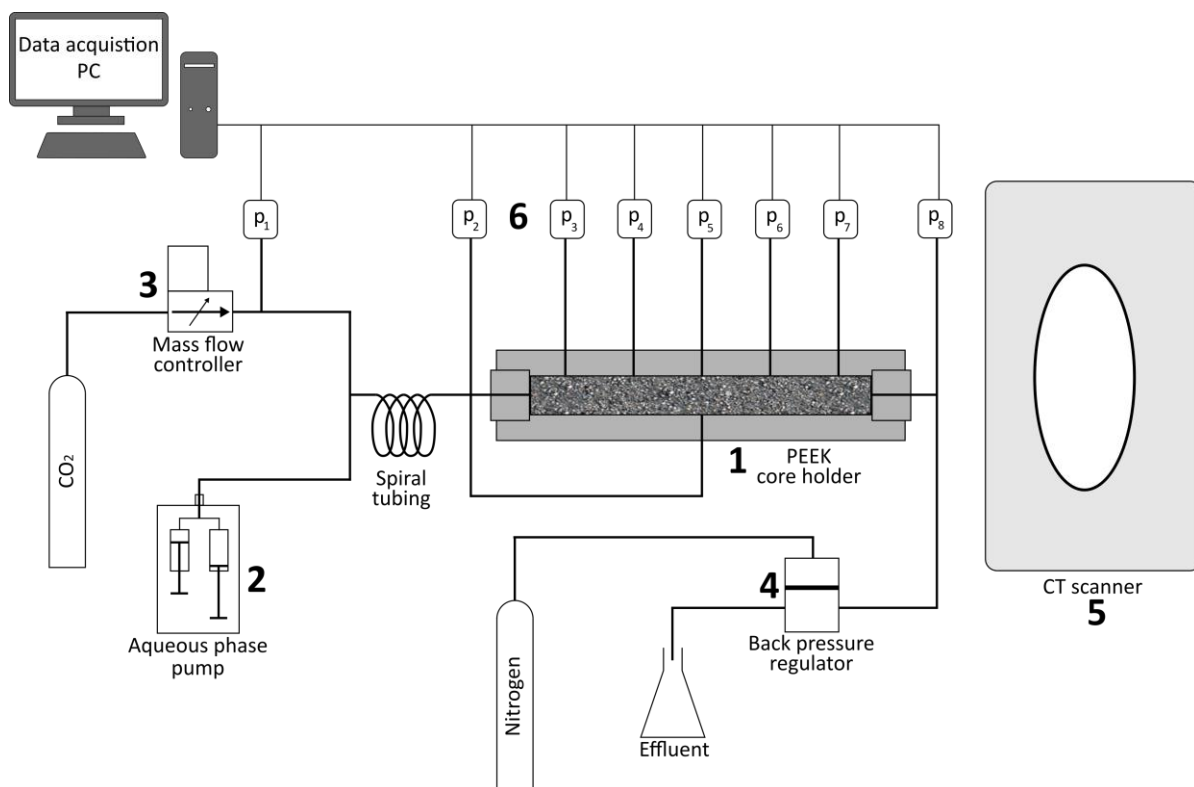


**Figure 1:** Schematic overview of experimental setup used in CT assisted coreflood experiments

**Table 1:** Overview of the components of the coreflooding setup

Number	Description
1	PEEK core holder
2	Quizix QX1500 aqueous phase pump
3	Bronkhorst ELFLOW CO <sub>2</sub> mass flow controller
4	Mity Mite S-91W back pressure regulator
5	Siemens SOMATOM Definition CT scanner
6	Keller PA33X pressure transducers

In its current form, the setup is meant for use at ambient temperatures at pressures up to 100 bar. The core holder is capable of withstanding elevated temperatures up to 90 °C, but this would require heating elements that do not cause any CT scanning artefacts. Tubing and connections in direct proximity to the core holder are also made of PEEK such that these also do not cause scanning artefacts. Most of the setup is installed on the sliding table of the CT scanner and can thus slide back and forth during the scanning process. A photograph showing the assembled setup is given in Figure 2.



**Figure 2:** Photograph of the coreflooding setup in the CT scanner

---

### 3 DEGASSING KINETICS OF HIGH SALINITY GEOTHERMAL FLUIDS

The content of this chapter has been accepted for publication as: Boeije, C.S., Weinzierl, W., Zitha, P.L.J. and Pluymakers, A.H.M., “Degassing kinetics of high salinity geothermal fluids”, *European Geologist Journal*, Special Issue on Geothermal Energy

Data associated with this publication are available from the following repository: “REFLECT deliverable 2.2: Report on gas solubility and degassing kinetic (type C)”, <https://doi.org/10.4121/77e70250-9c14-413e-baaf-595580215cc6>

#### ABSTRACT

The production of geothermal fluids can be adversely affected by the formation of free gas bubbles (degassing). Decreasing pressures can cause dissolved gas to exsolve, which can reduce water production. This study aims to improve the understanding of the conditions under which free gas nucleates in geothermal reservoirs. The focus is on CO<sub>2</sub> degassing from brines with varying salinity. We report a series of depressurization experiments at high pressure and temperature using a cell that allows for visual monitoring of the degassing process using a high-speed camera along with pressure and temperature logging. A geochemical model was created for simulating the degassing behaviour at the same conditions as those used in the experiments, thus allowing for direct comparison.

#### 3.1 INTRODUCTION

Degassing has several implications in subsurface flow applications such as production of hydrocarbons or geothermal fluids. Free CO<sub>2</sub> bubbles can cause more favourable conditions for the precipitation of calcium carbonate scale during both oil production (Cosmo et al., 2019; Fu et al., 2013) and production of geothermal brines (Arnórsson, 1989; Stefánsson et al., 2016). Chemically active gases like CO<sub>2</sub> and H<sub>2</sub> can also cause corrosion in both oil and geothermal wells (Pátzay et al., 1998).

In exploration of geothermal sites, the presence of degassing is also used as a marker for the potential of the site to contain geothermal resources (Rodríguez et al., 2021). Surveys of CO<sub>2</sub> degassing in soils have been used for this purpose in particular (Chiodini et al., 2007; Frondini et al., 2009). Furthermore, regions of high degassing rates are also found to indicate the presence of high-permeability faults (Peiffer et al., 2018). Finally, the presence of free gas bubbles can also lead to reduction of the water relative permeability of the reservoir as the bubbles take up space thereby limiting the ability for the water to flow. This was assumed to have happened in the the Groß Schönebeck field in Germany, which lead to a reduction in production index (Blöcher et al., 2016).

This study aims to improve the understanding of the formation of free CO<sub>2</sub> bubbles from fluids during a depressurization process, under geothermal reservoir conditions. The main research topic that is addressed is the dependency of the bubble point pressure on various parameters such as temperature and brine salinity.

#### 3.2 MATERIALS AND METHODS

Experiments performed in this study focus on the formation of free CO<sub>2</sub> bubbles during depressurization, mimicking the changes in pressure encountered in a geothermal well. The experiments were done at temperatures ranging from 40 to 150 °C. This temperature range

implies that these experiments are representative of low enthalpy geothermal sites (Chandrasekharam and Bundschuh, 2008).

### 3.2.1 Experimental setup

The experimental setup depicted in Figure 3 consists of the following components:

- A Vindum Engineering VP1-12K-HC dual piston aqueous phase pump allows for injecting water at high pressure.
- A Proserv Prolight 002990 titanium transfer vessel with a magnetic stirrer is used for creating gas-liquid mixtures.
- A titanium, high-pressure visual cell with two sapphire sight glasses (30 mm diameter) on either side to allow for visualization of the flow inside. The cell is cylindrical and has a 30 mm diameter and a depth of 10 mm. Fluid inlet and outlet are located at side and top of the cell respectively. A LED light source is installed to allow for uniform illumination of the cell's inner volume.
- A heating spiral is wrapped around the cell so that it can be heated up to the desired temperature in combination with a PID thermo-controller.
- A Photron FASTCAM Nova S6 camera is installed in front of the cell's window for high-speed imaging of the contents of the cell. This camera is used here at a rate of 500 frames per second. The camera is paired with a Laowa 100 mm f/2.8 2x Ultra Macro APO lens.
- A Sensata 84HP pressure transducer is connected to the cell to monitor the pressure during the experiments at a frequency of 100 Hz.
- Two thermocouples are connected to the cell as well: one for connecting to the thermo-controller and one to a data acquisition PC.
- A second Vindum Engineering VP1-12K-HC pump is used downstream of the cell in fluid receiving mode to reduce the pressure in a reproducible manner.
- Thicker tubing is installed downstream of the cell, which acts as a vessel for the hot fluids to cool down.
- A hardware switch is connected to both the camera and the data acquisition PC and is used to simultaneously stop the pressure and image recording, thus allowing for synchronisation between the two.



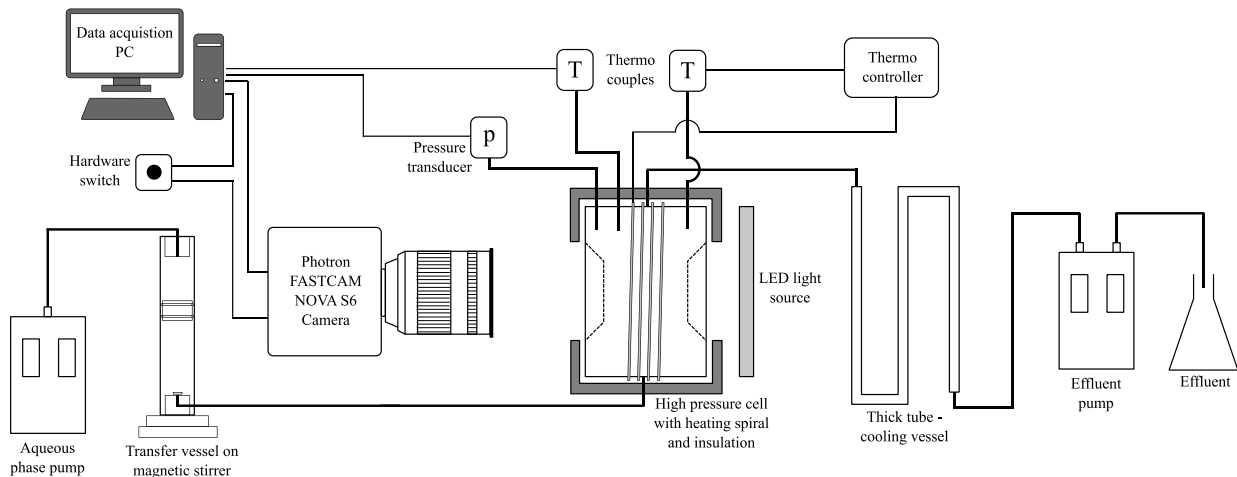


**Figure 3:** Schematic of experimental setup

### 3.2.2 Experimental procedure

Brine and CO<sub>2</sub> are premixed in the desired proportions and pressure in the transfer vessel and then homogenised using a magnetic stirrer. The visual cell is initially filled and pressurised using the same brine. The initial pressure is based on the predicted bubble point pressure from the model and is chosen to be significantly higher than this value. The brine-CO<sub>2</sub> mixture can then be pumped from the vessel into the cell, displacing the initial brine in the cell. Five times the cell's volume of the CO<sub>2</sub>-brine mixture is injected into the cell to ensure the cell contains the correct CO<sub>2</sub> concentration. Next the cell is heated to the desired temperature. The CO<sub>2</sub>-fluid mixture inside the cell is continuously monitored during both the filling and heating stage. Subsequently, the depressurization is performed by letting the downstream pump receive fluid from the cell. The receiving rate is scheduled such that the pressure reduction rate is gradual. The full depressurisation process takes approximately 40 seconds to complete, which coincides with the time it takes to fill up the camera's memory buffer. Once the pressure has been reduced sufficiently, free gas bubbles will start to form within the cell. The pressure at which the first gas bubbles are observed is the bubble point pressure and this pressure is the main result that is analysed in this study.

### 3.2.3 Data analysis methods

The main results from each experiment are a set of images that show the emergence of bubbles during the degassing process and the accompanying pressure log. An image analysis routine was developed using the MATLAB Image Processing Toolbox to identify individual bubbles and their properties such as size and growth rate. Since the images captured during the experiment and the pressure log are synchronised, the bubble data from the analysed images are combined with the pressure data to determine at which pressure bubbles are formed during the degassing process.

The image analysis consists of the following steps: first the background image (i.e., the image at the start of the experiment before bubble formation) is subtracted, resulting in net images with bubbles showing up as regions of high intensity. These net images are then converted to a binary format. Individual bubbles are identified in these images using MATLAB's

regionsprops function. Finally, the number of bubbles (i.e. individual regions) are counted on each image and can thus be plotted as a function of pressure.

### 3.2.4 Overview of experiments

Table 2 shows an overview of the experiments that were carried out within this study and lists their experimental conditions. Different brine compositions, temperatures and CO<sub>2</sub> concentrations were studied. For some of the experiments this means that CO<sub>2</sub> can already start forming bubbles while it is in its supercritical state, since the critical point is at:  $p_{crit,CO_2} = 73.8$  bar,  $T_{crit,CO_2} = 31.0$  °C.

**Table 2:** Overview of experimental conditions for elevated temperature experiments.

Brine composition	Temperature (°C)	Initial CO <sub>2</sub> concentration [mol/kgw]
1 M NaCl	40, 60, 100, 150	0.20
1 M NaCl	40, 60, 100	0.50
1.5 M CaCl <sub>2</sub> + 2 M NaCl	40, 60, 100, 120	0.15

### 3.2.5 Model description

This study mainly focuses on determining the bubble point pressure as a function of the studied parameters. The experimental results are compared to a geochemical model, which predicts the solubility of CO<sub>2</sub> in brine. This model uses the R coupled version of PHREEQC (De Lucia and Kühn, 2021). PHREEQC (pH-REdox-EQuilibrium) itself is a software package for simulating chemical reactions and transport processes (Parkhurst and Appelo, 2013).

At low pressures and following Henry's law the molar fraction of CO<sub>2</sub> in the aqueous phase depends on the partial pressure of the gas phase ( $P_{CO_2(g)}$ ) divided by Henry's constant  $K_H$ :

$$x_{CO_2}^{aq} = \frac{P_{CO_2(g)}}{K_H} \quad (1)$$

For high pressures the partial pressure needs to be replaced by the fugacity:

$$x_{CO_2}^{aq} = \frac{\phi P_{CO_2(g)}}{K_H} \exp\left(\frac{-v_{CO_2}}{RT}(P_{CO_2} - 1)\right) \quad (2)$$

where  $\phi$  is the fugacity coefficient of CO<sub>2</sub>. This can be computed by an Equation of State (EoS: (Duan and Sun, 2003; Peng and Robinson, 1976) or any other variant of a cubic or virial EoS); the exponential term is often called "Poynting correction";  $v_{CO_2}$  is the partial molar volume of CO<sub>2</sub> (aq) averaged over the  $P$  range  $[1, P_{CO_2}]$ . In the following,  $v_{CO_2}$  is equal to 0.032 L/mol (Spycher et al., 2003). At specified pressure and temperature conditions the PHREEQC model requires CO<sub>2</sub> fugacities as an input, which were computed with individual EoSs.

---

### 3.3 RESULTS AND DISCUSSION

#### 3.3.1 Comparison of experimental and modelled bubble points

Figure 4 shows the modelled  $\text{CO}_2$  solubility in 1 M NaCl brine as a function of pressure and temperature with input  $\text{CO}_2$  fugacities computed using an EoS described by (Duan and Sun, 2003). The contours in the plot are iso-solubility (mol/kgw). Experimentally determined bubble point pressures for this same brine are given in the same plot for comparison for both the 0.20 and 0.50 mol/kgw  $\text{CO}_2$  concentrations, which is why these contours are plotted using thicker lines. For the higher concentration experiments, the measured bubble points coincide fairly accurately with the predicted solubility, that is, the measurements are close to the 0.50 mol/kgw contour. This is not the case for the 0.20 mol/kgw experiment, where the measured bubble points are significantly lower than the model predicts. Measured bubble points here are between the 0.10 and 0.15 mol/kgw contours. An even better fit to the high concentration experiments can be obtained by using another EoS. Here we use the volume translated version of the Original Soave-Redlich-Kwong (SRK: (Soave, 1972)) EoS as described by (Le Guennec et al., 2016). In this case, the EoS's parameter values are fitted to the experimental data to obtain an improved match between experiment and model, as shown in Figure 5. Visual observation of the model prediction shows a better fit for the 100 °C experiment compared to the Duan and Sun EoS. Still, a good fit was not found for the lower concentration experiment, where data points remain significantly lower than the model predicts. The experimental approach can introduce a certain degree of error in the results, which may help explain the observed deviations between experiments and model. In order to assess the impact of the experimental approach, the experiments were first repeated using the same conditions. A comparison between the original and repeat experiments allows for determining whether the experimental procedure was carried out correctly as both experiments should ideally give the same results. Both sets of experiments were found to yield very similar results with variations in bubble point pressure limited to just 1 bar. Therefore, the experiments are considered to have been performed correctly. Secondly, the image analysis procedure was changed by lowering the threshold in the binary conversion step. This implies that smaller bubbles can be picked up earlier, but also that noise can erroneously be identified as bubbles. This still only caused very small deviations in the obtained bubble points, again with differences of around 1 bar compared to the values found earlier. So neither the repeat experiments, nor the change in the image analysis are sufficient to explain the discrepancy between measurement and model prediction and thus requires further investigation.

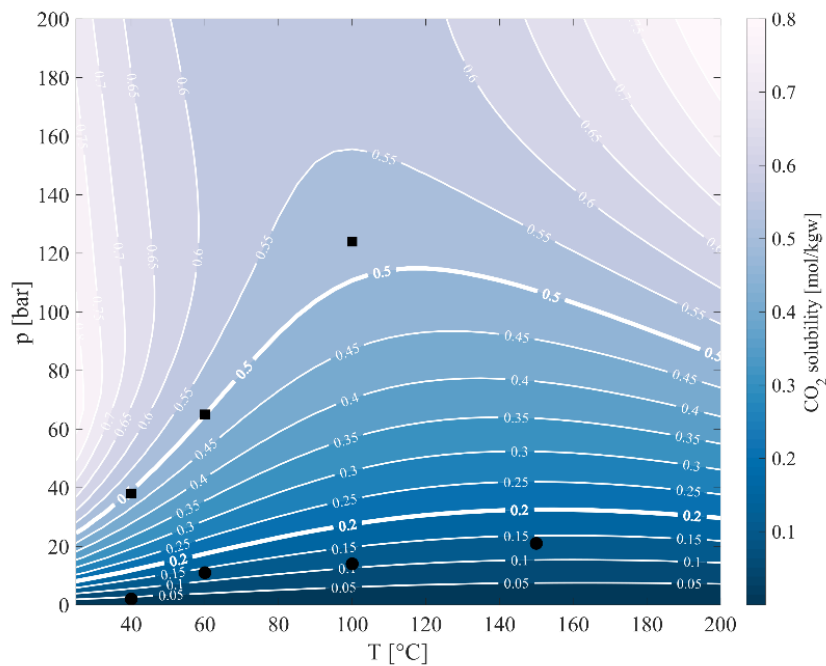


**Figure 4:** P-T dependence of the CO<sub>2</sub> solubilities in a 1 M NaCl brine solution. Results are obtained with PHREEQC and CO<sub>2</sub> fugacities computed using the Duan and Sun (2003) EoS. Experimentally obtained bubble points are also given for both the 0.20 mol/kgw (●) and 0.50 mol/kgw (■) CO<sub>2</sub> concentrations.

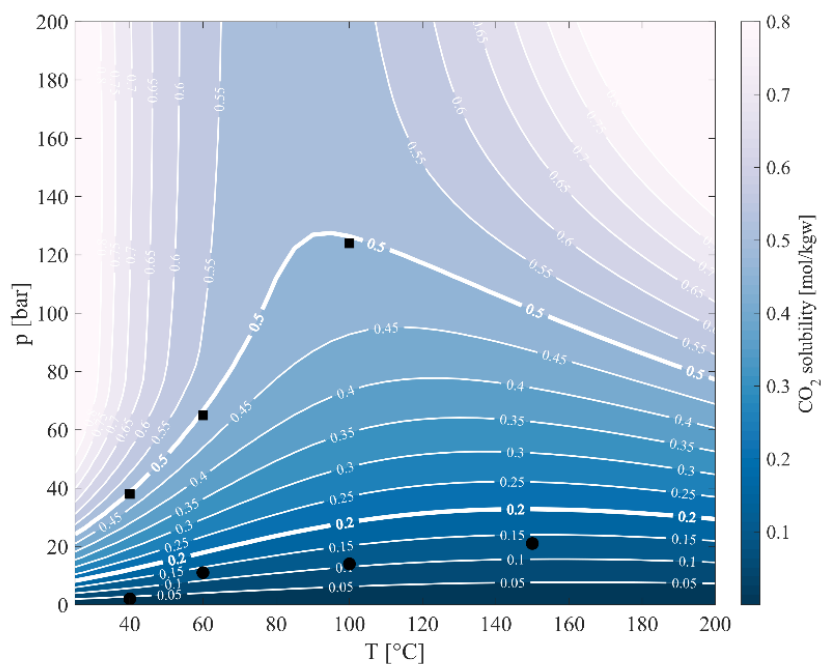


**Figure 5:** P-T dependence of the CO<sub>2</sub> solubilities in a 1 M NaCl brine solution. Results are obtained with PHREEQC and CO<sub>2</sub> fugacities computed using the volume translated SRK EoS. Experimentally obtained bubble points are also given for both the 0.20 mol/kgw (●) and 0.50 mol/kgw (■) CO<sub>2</sub> concentrations.

Figure 6 shows the model prediction of CO<sub>2</sub> solubility for the higher salinity brine (1.5 M CaCl<sub>2</sub> + 2 M NaCl) using the EoS of Duan and Sun along with the experimentally obtained bubble points using a CO<sub>2</sub> concentration of 0.15 mol/kgw. The lower concentration compared to the experiments using the 1 M NaCl brine was chosen here due to the model predicting significantly lower CO<sub>2</sub> solubility here. Results are thus compared to the 0.15 mol/kgw solubility contour, hence the increased line thickness for this contour.

Experimentally determined bubble point pressures found here agree reasonably well with the model predictions, although the deviations increase with increasing temperatures. The model also predicts increased CO<sub>2</sub> solubility for this concentration at temperatures beyond 100 °C. This behaviour was not found in the experiments, as the bubble point pressure at 120 °C is significantly higher than that at 100 °C. Additional experiments at higher temperatures are recommended to validate the model predictions.

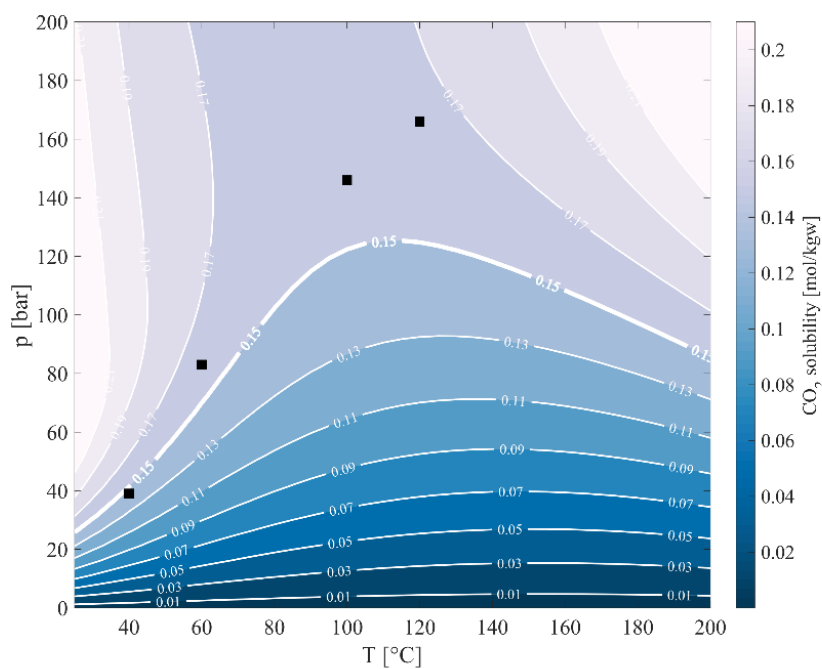


**Figure 6:** P-T dependence of the CO<sub>2</sub> solubilities in a 1.5 M CaCl<sub>2</sub> + 2 M NaCl brine solution. Results are obtained with PHREEQC and CO<sub>2</sub> fugacities computed using the Duan and Sun (2003) EoS. Experimentally obtained bubble points are also given for a CO<sub>2</sub> concentration of 0.15 mol/kgw (■).

### 3.3.2 Gaseous vs. supercritical bubbles

As mentioned above, some experiments performed here already have bubbles performing above the critical point of CO<sub>2</sub>. This is especially true at higher temperatures and CO<sub>2</sub> concentrations. Figure 7a and b show the bubbles for the experiments using the 1 M NaCl brine with 0.5 mol/kgw CO<sub>2</sub> concentration at 40 and 100 °C respectively. At 40 °C, bubbles only start forming at a pressure of ~40 bar, which means that here bubbles are gaseous, as the pressure is below the critical point. This results in fairly large bubbles that quickly rise up through the aqueous phase. For the 100 °C experiment, the bubbles already start forming at a pressure of ~125 bar, which is above the critical point of CO<sub>2</sub>, and thus bubbles are supercritical here. These bubbles are much smaller compared to the gaseous bubbles at lower

temperatures, which causes them to be much less buoyant and not to rise as fast inside the cell. The rate of bubble formation is also much larger for supercritical bubbles, as shown in Figure 8, which shows the observed number of bubbles as a function of pressure. Almost all of the supercritical bubbles form instantly as the bubble point is reached, obscuring the entire visual window and thus making it hard to distinguish individual bubbles. The gaseous bubbles at lower temperatures form far more gradually, starting with only a few bubbles near the bubble point and then gradually increasing as the pressure is reduced further.

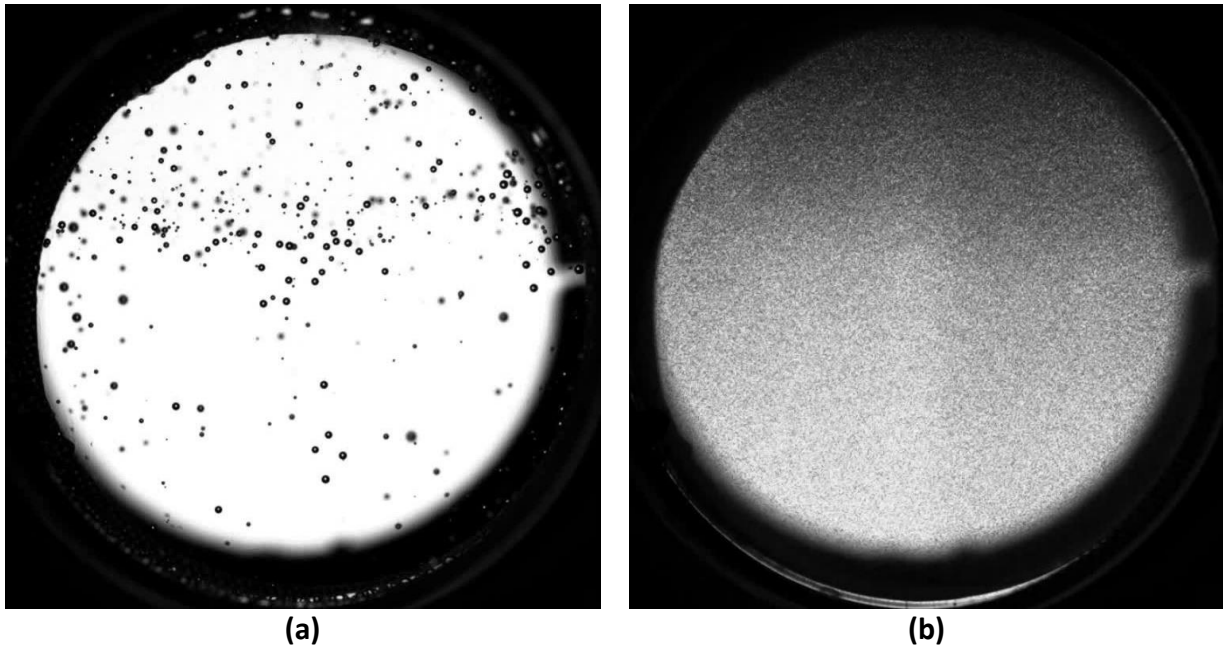


**Figure 7:** Experiments using 1 M NaCl brine and 0.5 mol/kgw CO<sub>2</sub> concentration showing (a) gaseous bubbles at 40 °C and (b) supercritical bubbles at 100 °C.

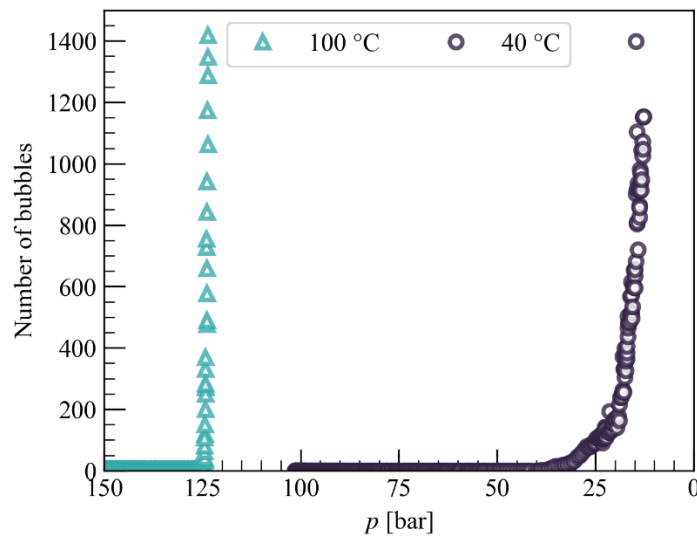


**Figure 8:** Number of bubbles vs. pressure for the experiments using 1 M NaCl brine and 0.5 mol/kgw CO<sub>2</sub> concentration at 40 and 100 °C respectively.

---

### 3.4 CONCLUSIONS AND RECOMMENDATIONS

- For the 1 M NaCl brine, the bubble point of a mixture with a high, 0.50 mol/kgw, CO<sub>2</sub> concentration, a good match is found between experiments and model for the investigated pressure and temperature conditions using either the Duan and Sun or volume translated SRK EoS model.
- At lower CO<sub>2</sub> concentrations, significant differences are found between the model and experiment. These deviations may be caused either by errors in the experimental approach or the model. Further evaluation of the degree to which these errors affect the results is recommended. The model description may also be improved by using pressure or temperature dependent formulations for certain physical parameters.
- The higher salinity brine (1.5 M CaCl<sub>2</sub> + 2 M NaCl) has approximately three times lower CO<sub>2</sub> solubility compared to the 1 M NaCl brine. A good match is found for experiment and model for this brine using a CO<sub>2</sub> concentration of 0.15 mol/kgw, although deviations between experiments and the model increase at higher temperatures.
- Supercritical bubbles are much smaller and also form in much greater numbers at or near the bubble point pressure compared to gaseous bubbles.
- Further experiments at higher temperatures are required to validate the solubility behaviour that is predicted by the geochemical model. The experimental approach (i.e. high-speed imaging inside a visual cell) used here is well suited for performing experiments at higher temperatures, although some parameters can be improved upon to capture the process in greater detail. These include running the camera at a higher frame rate and using a more zoomed-in view of the visual cell. This is especially relevant when observing the formation of the supercritical bubbles, which are very small and form almost instantaneously in large quantities.

---

## 4 REDUCTION OF EFFECTIVE PERMEABILITY DUE TO CO<sub>2</sub> DEGASSING

### ABSTRACT

Geothermal fluids are often saturated with gasses such as CO<sub>2</sub> and N<sub>2</sub>. Production of these fluids from the reservoir leads to a decrease in pressure towards the extraction well. This disturbs the state of equilibrium the geothermal water is in with its dissolved components, which for gas can lead to exsolution. The exsolved gas bubbles can block the pores of the reservoir rock and therefore reduce its effective permeability. As permeability reduction occurs mainly near the extraction well it can reduce production of geothermal waters substantially. This paper is aimed at experimentally investigating the conditions at which the onset of degassing starts and quantitatively assess any associated permeability decrease. Knowledge on these parameters will enable operators to adapt their operation procedures in order to ensure long-time reservoir permeability.

This paper reports core-flood experiments where tap water containing dissolved carbon dioxide was injected into a vertically oriented Berea (140 millidarcy) sandstone core at different conditions (temperature up to 70 °C, pressure up to 80 bar and brine salinity up to 1.5 M CaCl<sub>2</sub> + 2 M NaCl). Here we find that using a higher salinity brine leads to a higher degassing pressure, which deviates from the Van 't Hoff equation. Using the highest salinity brine here results in up to 50% deviation in the degassing pressure compared to tap water. However, this does not affect the ultimate reduction in effective permeability of the medium which was found to be independent of the used aqueous phase. We performed additional CT assisted coreflood experiments using a horizontally oriented Berea core to provide further insight into the distribution of fluids inside the core. The CT assisted coreflood experiments showed a fairly stable free gas front at lower CO<sub>2</sub> concentrations. At higher concentrations, the effects of gravity override become more pronounced, but the extent to which the water relative permeability drops in the regions of the core where degassing occurs is found to be fairly stable. This is also the case for the water saturation in these degassed zones, which does not drop below a value of 0.63. Further reduction of the pressure leads to movement of the degassing front upstream into the core. This also explains why the permeability decrease observed in all the experiments quickly reaches a plateau and does not reduce further at lower pressures.

### 4.1 INTRODUCTION

Geothermal waters can have various gases in solution, such as CO<sub>2</sub> and N<sub>2</sub> (Haizlip et al., 2016). During the production of these waters, a change in pressure and temperature will occur in the vicinity of the extraction well. These changes disturb the equilibrium the water is in with its dissolved gases (Pátzay et al. (1998) and can result in degassing (Blöcher et al. (2016). The exsolution of gas from the solution will lead to free gas bubbles (Boeije et al., 2022a), effectively leading to a two phase gas-liquid flow system. The effective pore space available for the flow of water is reduced, as part of the total pore space is taken up by gas. Therefore the water relative permeability of the liquid phase will decrease (Bear, 2013) , (Zuo and Benson, 2014), (Mahabadi et al., 2018).

This most likely occurred at the Groß Schönebeck geothermal site in Germany, where the productivity index (PI) dropped from 8.9 m<sup>3</sup>/(h·MPa) to 0.6 m<sup>3</sup>/(h·MPa), from June 2011 and November 2013. The decrease in permeability due the presence of free gas was proposed as



one of the possible causes for the productivity index decline (Blöcher et al., 2016). Exsolution of CO<sub>2</sub> also causes a significant contribution to global carbon emissions (Tamburello et al., 2018). Another problem associated to degassing is that the release of presence of free gas enhances the precipitation of minerals such as calcite. Various studies report an increase in the rate of calcite scaling in the presence of free CO<sub>2</sub> (Cosmo et al., 2019). This can lead to a substantial reduction of the permeability (Flores et al., 2017), (Aminu et al., 2018). Still, calcite scaling is found to be most problematic in or near the production well and not affect the permeability further in the reservoir due to the larger pore volume of the reservoir that can cope with the deposition of scales (Arnórsson, 1989).

Gas exsolution also plays a role in geological storage of CO<sub>2</sub> when the gas is dissolved in formation brine where the exsolved CO<sub>2</sub> can lead to very low water and gas relative permeability (Zuo et al., 2012). On the other hand, maintaining the CO<sub>2</sub> in solution can increase porosity and thus storage capacity due to calcite dissolution (Lamy-Chappuis et al., 2014).

Despite the many observations suggesting a direct link of PI decline and release of dissolved gas, data supporting this idea and a coherent picture about the process are lacking. This study aims to address the following question:

*To which extent is the flow of water in rocks limited by release of free gas from a saturated water/gas solution?*

by experimentally investigating at which conditions the onset of the degassing process starts and what the effect of the degassing process on the effective water permeability. Factors influencing the degassing process and its effect on the permeability will be analyzed and discussed. These factors include the rock pore scale characteristics, temperature, and salinity.

## 4.2 MATERIALS AND METHODS

This study comprises series of coreflood experiments in which CO<sub>2</sub> and an aqueous phase were co-injected into a rock core. In the first series, two rocks samples were used, having either high permeability (Bentheimer sandstone, 2.3 D) or lower permeability (Berea sandstone, 140 mD). In this series, the temperature was set at 30 °C. The second series investigated a range of temperatures (up to 90 °C) and pressures (up to 80 bar) using only the low permeability Berea core sample. In the third series, the effect of salinity was studied by using a higher salinity brine as the aqueous phase (1 M NaCl or 1.5 M CaCl<sub>2</sub> + 2 M NaCl). Finally, a set of CT assisted corefloods was performed, where the CT scans allow for visualizing the interior of the core at various stages during the injection process. This section outlines the experimental setup used in this study and the experimental procedure.

### 4.2.1 Experimental setup

Figure 9 shows a schematic of the experimental setup used for the experiments outside the CT scanner using the vertically oriented core. CO<sub>2</sub> supplied from a bottle was injected into the core using a gas booster and mass flow controller (Bronkhorst ELFLOW). The gas injection pressure was monitored using an absolute pressure transmitter (Keller PA33X, labelled  $p_1$  in the schematic). A Quizix QX-1500 dual piston pump was used to inject the aqueous phase, note that either tap water or a higher salinity brine is used. Tap water was used instead of

demineralized water to minimize the risk of the dissolution of clay particles from the cores. The rock core (40 cm long and 4 cm in diameter) is placed in a PEEK core holder, which is installed vertically in an oven that can be set to the desired temperature. Before reaching the rock core the fluids have to flow through a length of tubing in the oven (approximately 2 m in length). This allows them to reach the desired temperature and gives the CO<sub>2</sub> time to mix with the water, such that only a single phase (water with dissolved CO<sub>2</sub>) enters the core. The final length of tubing before the inlet of the core holder is transparent. This enables visual observation of the flowing fluids to ensure that the fluids are mixed properly before entering the core and no free gas bubbles are present. The fluids enter the core at the bottom, flow vertically through the core's pore space and exit at the top. A series of absolute pressure transmitters (Keller PA33X, p<sub>2</sub> to p<sub>8</sub> in the schematic) is installed along the length of the core that allow the monitoring of the pressure at various positions during the experiment. The desired operating pressure is set using a gas-controlled back-pressure regulator (Mity Mite S-91W) installed downstream of the core.

An additional set of corefloods was performed during which CT scanning was employed to determine the saturations of gas and liquid inside the rock core. The main change is that for these experiments, the core had to be oriented horizontally due to limitations of the CT scanner (Siemens Somatom Volume Zoom). These experiments were all performed at ambient temperature so no heating elements were required. Besides these changes, all of the experimental equipment used in the previous experiments could also be used here. Further details of this setup have been discussed above in Chapter 2 of this report. These experiments were done with a Berea core using tap water at pressures up to 50 bar. An overview of all the experiments performed within this study is given further down at the start of the Results section (cf. Table 3).

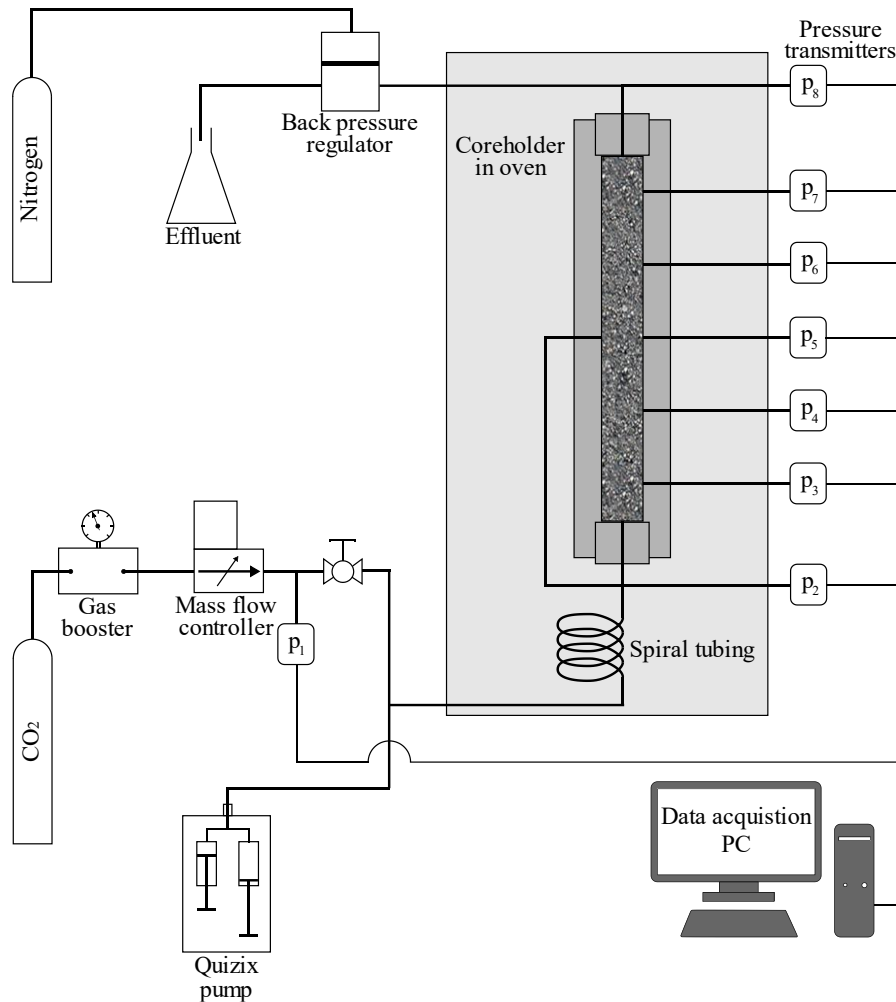


**Figure 9:** Schematic of experimental setup used in experiments outside CT scanner

#### 4.2.2 Experimental procedure

In all of the experiments carried out in this study, water and CO<sub>2</sub> are co-injected into the rock core. Different experiments allow for analyzing the effects of various experimental parameter such as temperature, rock type or salinity on the degassing process. All of the series of experiments discussed in this manuscript use a range of CO<sub>2</sub> concentrations. For each experiment, the initial back-pressure (*IBP*) was chosen sufficiently high such that the CO<sub>2</sub> fully dissolves in water, which means that high concentration experiments require a higher value of *IBP*. By lowering the back-pressure (*BP*) step by step, the point where the degassing starts, i.e. the degassing back-pressure (*DBP*), can be determined by monitoring the fluid pressure (*FP*) in the core. The formation of free gas is revealed by a significant rise of the *FP*. Further decrease in *BP* below the onset of degassing allows insight into how the presence of the free gas bubbles affect the water relative permeability of the core as the pressure drop increases further as the free gas saturation rises. A similar procedure was used by (Zuo et al., 2012) in which a brine/CO<sub>2</sub> solution was depressurized during core-flood experiments.

Between each experiment the core is flushed with water to get the remaining CO<sub>2</sub> out. This is done by first lowering the backpressure, which causes gas expansion, which in turn forces the gas to leave the core. Then the backpressure is increased while injecting water, which results in a higher CO<sub>2</sub> solubility, thus causing the remaining CO<sub>2</sub> to dissolve in the water.

The CT experiments are largely performed in a similar fashion, but here after every reduction of *BP* a CT scan is taken once a steady state has been reached. This provides additional information on the distribution of the fluids in the core that can be correlated to the differential fluid pressure logs.

### 4.2.3 Data analysis

The raw data obtained from each set of experiments consists essentially of the pressures measured at each pressure transducer taken at two second intervals. The difference between two adjacent pressure transducers combined with the difference in height gives the pressure gradient over an interval. To reduce the noise in the raw data it is edited using time averaging over 20 points. This improves the signal to noise ratio of the data significantly.

The results reported in this study are mostly pressure drops over the last section of the core as a function of the back-pressure. Since pressure is lowest in the last section degassing will start in this section. When a rapid increase of the pressure drop in the last section is observed, the *BP* measured at that point is taken as the onset of the degassing process or simply the degassing pressure (*DBP*).

The experimentally obtained *DBP* is then compared with the prediction of the bubble point from thermodynamic theory applied to the CO<sub>2</sub>-water system. The bubble point pressure can be estimated using Henry's law (Eq (3)).

$$H_0 = \frac{s_{CO_2}}{p} \quad (3)$$

where  $H_0$  is the value of Henry's constant at standard conditions [equal to 0.336 mol/(L·bar) for CO<sub>2</sub>],  $p$  is the pressure in bar and  $s_{CO_2}$  is the solubility of CO<sub>2</sub> in water at standard conditions in mol/L (Sander, 2015). The solubility of gases in water typically decreases as the temperature increases. The applicability of Eq. (3) can be extended to higher temperatures by using the Van 't Hoff equation, which gives Henry's coefficient as function of the temperature  $H(T)$  as:

$$H(T) = H_0 \exp \left[ -\frac{\Delta_{sol}H}{R} \left( \frac{1}{T} - \frac{1}{T_0} \right) \right] \quad (4)$$

where the term  $\Delta_{sol}H$  is the enthalpy of dissolution and  $T_0$  is the reference temperature taken here as 298.15 K.  $\Delta_{sol}H/R$  is independent of temperature and, for CO<sub>2</sub>, is equal to 2400 K (Sander, 2015). The Van 't Hoff equation is used throughout this manuscript to compare the observed bubble points with the theoretical predictions. The observed pressure gradients can also be used to determine the effective core permeability by applying Darcy's law (Eq. (5)).

$$k_{eff} = \frac{Q\mu_w L}{\Delta p_m} = k \cdot k_{rw} \quad (5)$$

where  $Q$  [m<sup>3</sup>/s] is the volumetric flux,  $\mu_w$  [Pa·s] is the water viscosity at the investigated temperature,  $\Delta p_m$  [Pa] is the measured pressure drop,  $L$  [m] is the length of the investigated section of the core over which the pressure drop is measured and  $k_{eff}$  [m<sup>2</sup>] is the effective permeability of the medium based on the measured pressure drop. In case of a two phase liquid-gas flow system, this is equivalent to the absolute permeability multiplied by the water

relative permeability. Thus in the experiments the value of  $k_{rw}$  can be calculated by comparing the measured pressure drop  $\Delta p_m$  in the two phase system with that of the single phase waterflood  $\Delta p_w$  (Eq. (6)). We have verified that for the flow rates used in this study the flow was in the laminar regime for which Darcy's law is valid.

$$k_{rw} = \frac{\Delta p_w}{\Delta p_m} \quad (6)$$

CT scans enable distinguishing of gas, liquid and the rock matrix within the core at various stages during the experiments as different materials lead to different levels of attenuation of the source radiation. This allows for determining the porosity and the fluid saturation within the core by using the method outlined in (Rangel-German et al., 1999). The porosity  $\varphi$  can be calculated as follows:

$$\varphi = \frac{CT_{wet} - CT_{dry}}{CT_{water} - CT_{air}} \quad (7)$$

Here  $CT_{wet}$  and  $CT_{dry}$  are the CT numbers (that is, the CT attenuation coefficients given in Hounsfield units) of a wet and dry core respectively (i.e. a core fully saturated with water and a core fully saturated with air).  $CT_{water}$  and  $CT_{air}$  are the CT numbers for water and air respectively, which are equal to 0 and -1000. In similar fashion, during the coreflood experiments, the water  $S_w$  and gas saturations  $S_g$  can be obtained as follows:

$$S_w = \frac{CT_{exp} - CT_{dry}}{CT_{wet} - CT_{dry}} \quad (8)$$

$$S_g = 1 - S_w \quad (9)$$

Here  $CT_{exp}$  is the CT number measured during the coreflood experiment. The saturation measurements are useful in determining to which extent gas bubbles need to be formed in order to cause a significant blockage effect within the core. The measured saturation values can be compared to literature values for water relative permeability. (Kapetas et al., 2017) have measured Brooks-Corey parameters for relative permeability of various rock types including the Berea sandstone used within this study thus these can be used for direct comparison with the measured saturation data. The Brooks-Corey water relative permeability  $k_{rw}$  as a function of the water saturation is as follows:

$$k_{rw}(S_w) = k_{rw}^0 \left( \frac{S_w - S_{wc}}{1 - S_{wc} - S_{gr}} \right)^{n_w} \quad (10)$$

Here  $k_{rw}^0$  is the end-point water relative permeability,  $S_{wc}$  is the connate water saturation,  $S_{gr}$  is the irreducible gas saturation and  $n_w$  is the Corey exponent. For Berea sandstone (Kapetas et al., 2017) found the following values for these constants:  $k_{rw}^0 = 0.39$ ,  $S_{wc} = 0.23$ ,  $S_{gr} = 0.12$  and  $n_w = 4.09$ .

### 4.3 RESULTS AND DISCUSSION

In this section, representative results of the experiments will be given and discussed. Since pressure is lowest towards the outlet of the core, this is the location where the first onset of degassing is expected to occur. This is why the results shown in this report are mostly pressure drops in the last two sections of the core. An overview of the conditions that were used for the various experiments is shown in Table 3.

**Table 3:** Overview of conditions used in the experiments

Rock type	$T$ [°C]	Aqueous phase	$s_{CO_2}$ [mol/L]
Berea	70	Tap water	0.2 – 0.8
Berea	70	1 M NaCl	0.2 – 0.8
Berea	70	1.5 M $CaCl_2$ + 2 M NaCl	0.2 – 0.6
Berea	20*	Tap water	0.3 – 1.3

\* These experiments were performed at ambient temperature with CT scans taken at various stages during the experiment

#### 4.3.1 Typical results

Results that are common throughout all the experiments are the pressure monitoring results. As mentioned in the experimental procedure in section 4.2.2, the degassing process is studied by lowering the absolute pressure at the end of the core (backpressure) in a stepwise manner. At some point the solubility limit is reached at the end of the core where the pressure is lowest causing free gas bubbles to form thereby increasing the pressure drop in the last section. An example of this is shown in Figure 10, which shows the backpressure and pressure drop in the last section for the experiment performed outside the CT scanner using a 1 M NaCl solution at 70 °C. The abrupt increase in the pressure drop indicated in the figure is the onset of degassing. In order to compare different experiments with each other, it is easier to express the pressure drop as an effective permeability of the medium by applying Darcy's law (Eq. (5)).

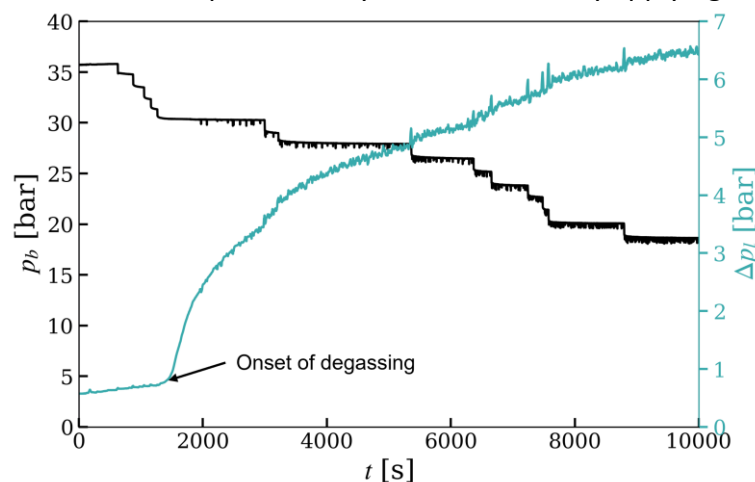


**Figure 10:** Example of pressure logs showing the backpressure ( $p_b$ ) and pressure drop over the last section of the core ( $\Delta p_l$ ) for the experiment using 1 M NaCl solution at 70 °C

### 4.3.2 Effect of brine salinity

In order to assess the influence of brine salinity on the degassing process, experiments have been performed using three different aqueous phases (tap water, 1 M NaCl and 1.5 M CaCl<sub>2</sub> + 2 M NaCl) at 70 °C. Here we first compare the results from the tap water and the NaCl brine experiments, which were both performed using CO<sub>2</sub> concentrations ranging from 0.2 to 0.8 mol/L to allow for direct comparison in the degassing pressure and the extent to which the effective permeability is reduced. Figure 11 shows a comparison of the development of effective permeability for the tap water and NaCl experiments. A clear shift in degassing pressure is found between both sets of experiments. The NaCl experiments lead to degassing pressures that were between 2.5 and 3.5 bar larger than the tap water experiments. The ultimate reduction in effective permeability is very similar for both sets of experiments though indicating that the bubble nucleation and bubble growth mechanism is not affected by the increased salt concentration.

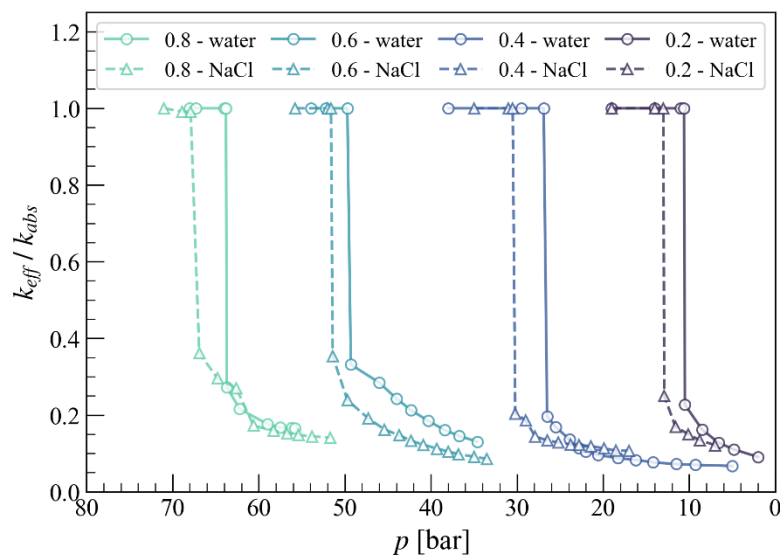


**Figure 11:** Comparison of effective permeability as a function of back-pressure at 70 °C for experiments using water and 1M NaCl as the aqueous phase. Legend indicates CO<sub>2</sub> concentration [mol/L]

Next, the higher salinity brine experiments (1.5 M CaCl<sub>2</sub> + 2 M NaCl) were performed. Effective permeability results of this are shown in Figure 12 along with the tap water results for direct comparison. Significantly larger deviations in the degassing pressure are found here with the differences increasing with increasing CO<sub>2</sub> concentrations. The largest difference found in this series is the 25 bar difference (52 vs. 77 bar) for the experiment using a CO<sub>2</sub> concentration of 0.6 mol/L. Because of this large increase in degassing pressure, the highest concentration used in the previous experiments using the 1 M NaCl brine of 0.8 mol/L could not be replicated here as it would require initial pressures beyond the limits of the equipment. For all three investigated concentrations, the degassing pressure is approximately 50% higher for the high salinity brine compared to the tap water experiments, which implies a significant reduction in CO<sub>2</sub> solubility when using this brine. The degree to which the effective permeability is altered at lower pressures is similar to that found for previous experiments using tap water (i.e. up to 90% reduction in effective permeability). So, to sum up, the reduction in final effective permeability is always the same and is not a function of the salinity, but the pressure at which the degassing begins is different.

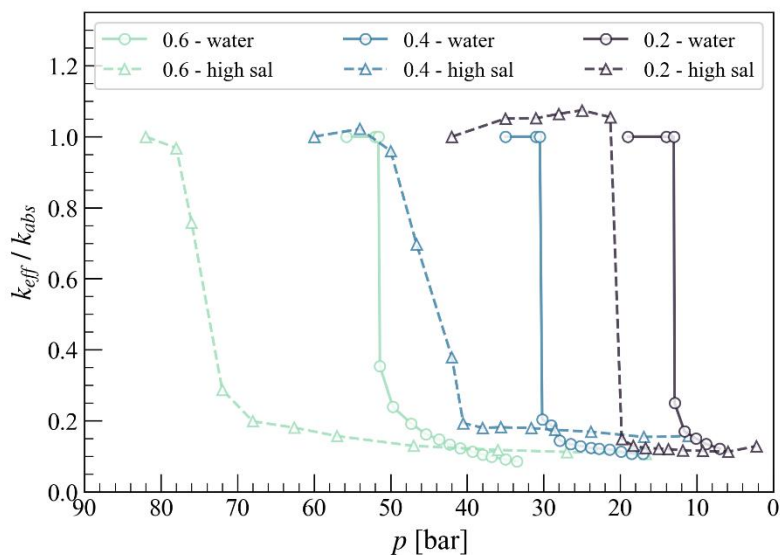


**Figure 12:** Comparison of effective permeability as a function of back-pressure at 70 °C for experiments using water and high salinity brine (1.5 M CaCl<sub>2</sub> + 2 M NaCl) as the aqueous phase. Legend indicates CO<sub>2</sub> concentration [mol/L]



The pressure at which the degassing starts has also been calculated using the Van 't Hoff equation (cf. Eq. (4)). This equation is only valid for pure CO<sub>2</sub>-water mixtures and does not take the brine salinity into account. Thus, this can be used to determine the extent to which the salinity affects the degassing pressure. An overview of the degassing onset pressures for the tap water, NaCl and high salinity experiments at 70 °C can be compared to the Van 't Hoff prediction in Figure 13. There is not much difference between the tap water and the NaCl experiments, with the latter actually showing a better match with Van 't Hoff theory. The presence of salts is not included in the model though, so the observed accurate fit between the experiments and model is believed to be a coincidence. The high salinity experiments show a much larger deviation from the theoretical prediction with increasing differences as the CO<sub>2</sub> concentration rises.

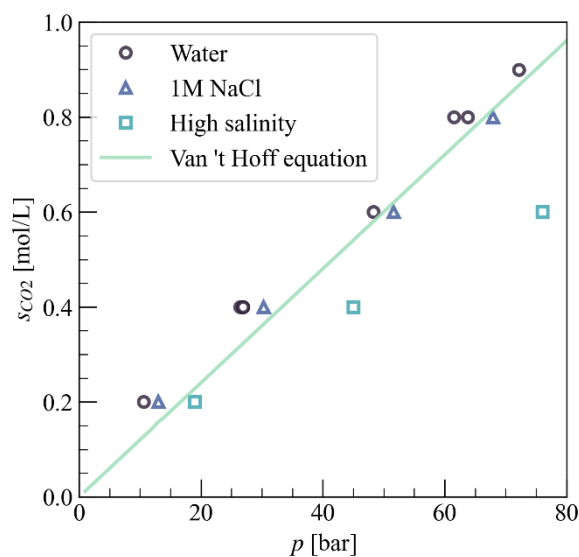
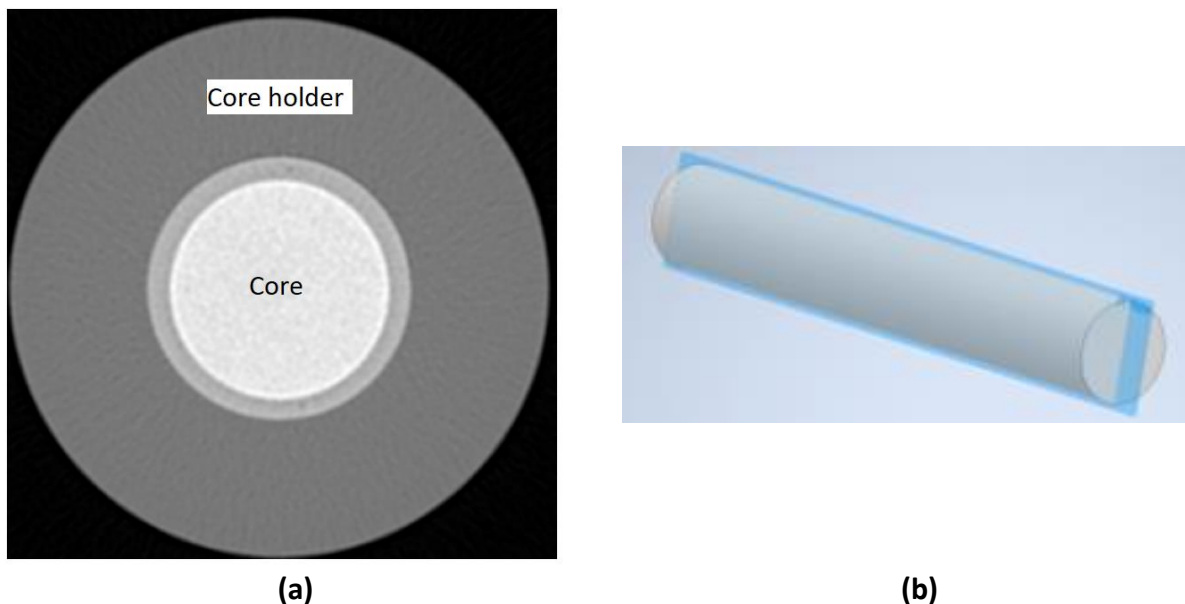


**Figure 13:** Onset degassing process of the water, NaCl and high salinity brine experiments versus the Van 't Hoff equation at 70 °C

### 4.3.3 CT experiments

The CT experiments are performed in a similar fashion compared to the previous experiments, but a CT scan is taken at various stages during the injection process, but always once a steady state has emerged in terms of pressure drop. The resulting CT scans are vertical slices through the horizontally oriented core. The entire setup is on a sliding table, which is used to move the core within the scanner. This allows for taking scans at many different locations within the rock core. A total of 661 scans are taken along the 40 cm core, with a spacing of 0.6 mm between scans. The resolution of the images is 0.195 mm. The entire process of taking these 661 slices takes approximately 10 seconds, so for experiments with slow moving fluids at steady state this is sufficient. An example of a single slice is given in Figure 14a, which shows a cross section of the core inside the core holder. The aim of the results in this report is to show the distribution of the fluids throughout the core. Therefore, the CT profiles shown below use the CT data on a vertical slice through the centre of the core as shown in Figure 14b.

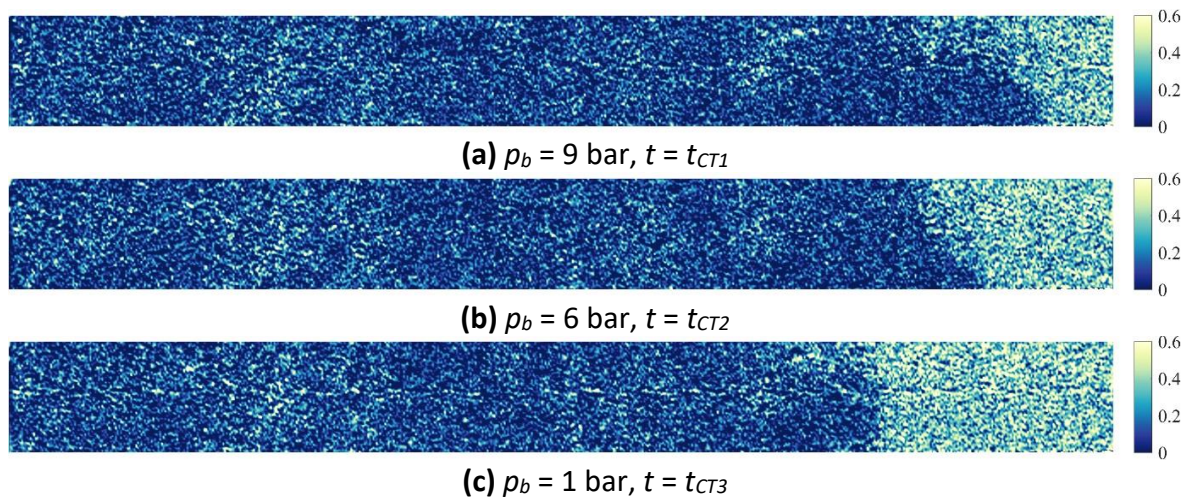
CO<sub>2</sub> concentrations within these experiments were chosen picked to be the same as those used in a previous set of experiments that were performed outside the CT scanner (Boeije et al., 2022b) to allow for direct comparison between the two.



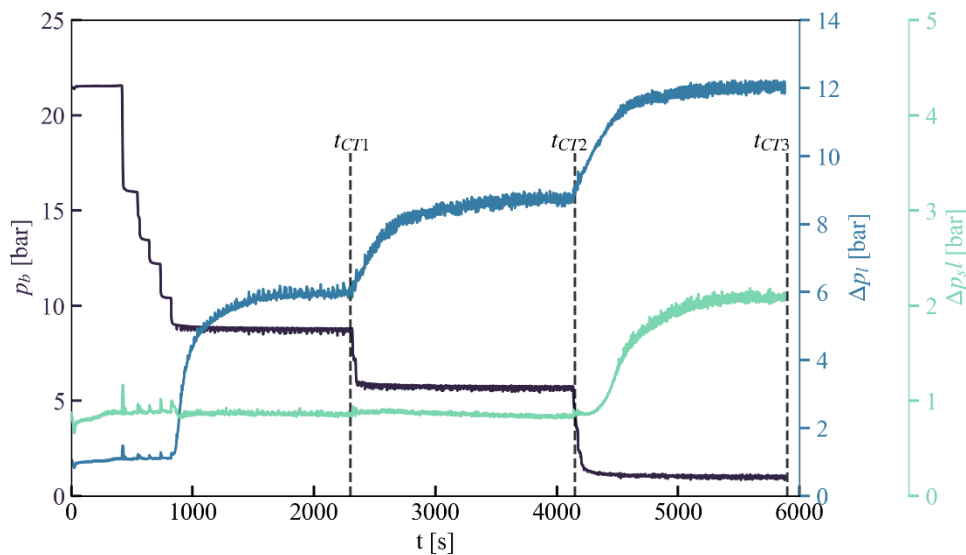
**Figure 14:** (a) Example of a CT slice showing a cross section of the core inside the PEEK core holder (b) vertical plane through center of core showing where results are plotted

Figure 15 shows a series of CT scans taken at different points in time during the experiment using a CO<sub>2</sub> concentration of 0.5 mol/L using tap water as the aqueous phase. The flow direction in these images is from left to right. These images show the gas saturation  $S_g$  on a vertical cross section through the horizontally oriented core at the indicated value of the back pressure. These values were obtained by combining the CT images of a fully dry core, a fully wet core and the core during the experiments by using equation (8) and (9). Similarly to the experiments outside the CT scanner, the primary focus here is on the last and second to last section of the core ( $x/L = 0.84$  up to 1 and  $x/L = 0.68$  up to 0.84 respectively), because the

effect of degassing is most prominent here. In these images, a free gas front moves upstream into the core as the pressure is reduced, which agrees with previous experiments outside the CT scanner. The gas front appears fairly stable with limited gravity override despite the horizontal orientation of the core. The points in time at which the scans are taken ( $t_{CT1, 2, 3}$ ) are also indicated in the pressure log of this experiment in Figure 16, which shows both the back pressure ( $p_b$ ) of the system as well as the pressure drops in the last ( $\Delta p_l$ ) and second to last section ( $\Delta p_{sl}$ ) of the core. The pressure logs for this experiment show similar behaviour to the previous experiment with an abrupt increase in pressure drop in the last section of the core below the degassing pressure (which in this case is approximately 9 bar,  $t \sim 900$  s in the figure). Further increase of the pressure drop in this section is found as the back pressure is reduced further with the pressure drop at the end of the experiment approximately 10 times higher compared to the single phase waterflood. In this final stage, the degassing front has moved upwards into the core and reaches the second to last section, where the pressure drop also starts to increase albeit not as much as in the last section. The increase in pressure drop is around a factor 2 for this section at the end of the experiment implying less free gas is present here.



**Figure 15:** Gas saturation at vertical slices through the core taken at indicated back pressure using a CO<sub>2</sub> concentration of 0.5 mol/L



**Figure 16:** Backpressure ( $p_b$ ) along with pressure drop in the last section ( $\Delta p_l$ ) and second to last section of the core ( $\Delta p_{sl}$ ) using a CO<sub>2</sub> concentration of 0.5 mol/L. CT scans are taken at  $t = t_{CT1}$ ,  $t_{CT2}$  and  $t_{CT3}$

At higher concentrations, the results look quite different. A representative result is the experiment using 0.9 mol/L of which the CT saturation profiles are shown in Figure 17. These saturation profiles suffer from significant gravity override caused by the horizontal orientation of the core and the density difference between the free gas and the aqueous phase. Degassing starts at  $p_b = 22$  bar for this concentration ( $t \sim 1800$  s in the figure) and free gas can already be found throughout the core at this pressure close to the top of the core. Because of this, the pressure drop does not only increase in the last section, but also an increase, albeit slight, can be found in the second to last section as well. Further increase in the second to last section is found when free gas starts blocking the entire section, which happens when  $p_b$  is reduced to 10 bar. For the last section of the core, the increase in pressure drop is similar to that observed in previous experiments, reaching a value around 10 times higher compared to the single phase waterflood at the end of the experiment.

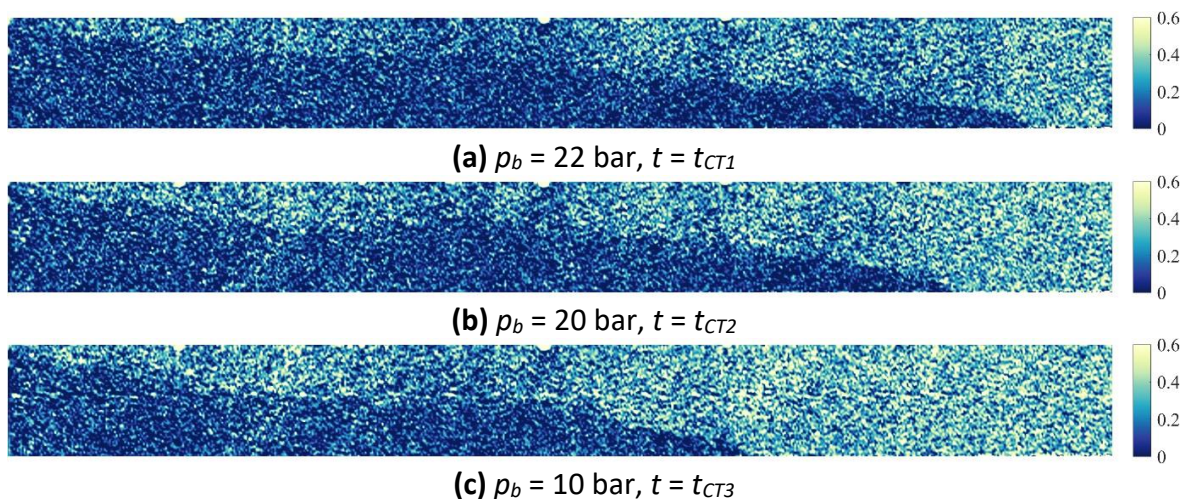


**Figure 17:** Gas saturation at vertical slices through the core taken at indicated back pressure using a CO<sub>2</sub> concentration of 0.9 mol/L

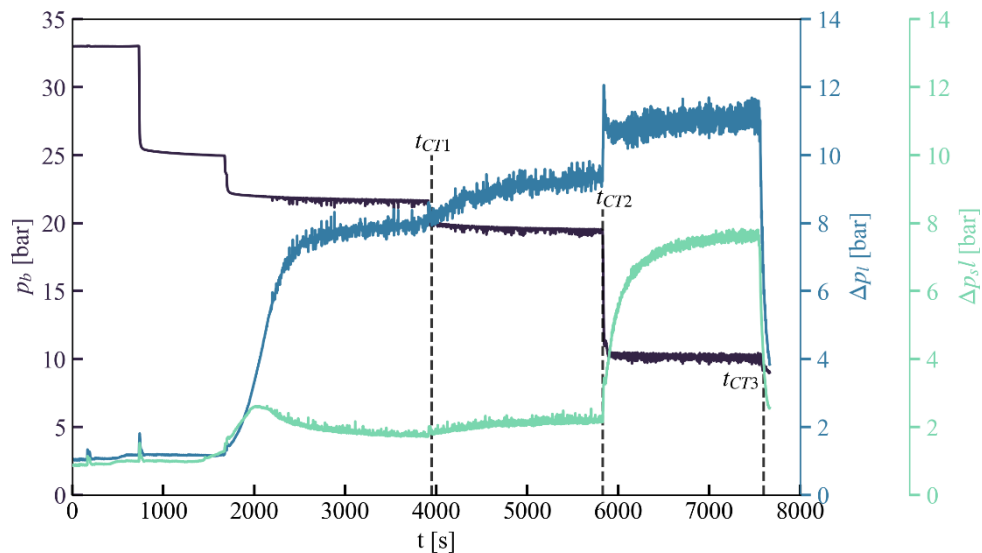


**Figure 18:** Backpressure ( $p_b$ ) along with pressure drop in the last section ( $\Delta p_I$ ) and second to last section of the core ( $\Delta p_{SI}$ ) using a CO<sub>2</sub> concentration of 0.9 mol/L. CT scans are taken at  $t = t_{CT1}$ ,  $t_{CT2}$  and  $t_{CT3}$

The pressure drop can also be related to a drop in the water relative permeability. As mentioned, for the Berea rocks the pressure drop increased by roughly a factor 10 in the last section when free gas has fully spread through the entire section. This implies a water relative permeability equal to 0.1. The average water saturation can also be determined by averaging the saturation values found from the CT scan in the section. Table 2 shows the water relative permeability  $k_{rw}$  and the average water saturation  $\langle S_w \rangle$  for all of the performed experiments in the last and second to last section of the core at the end of each experiment (i.e. using the lowest back pressure value). These values are compared to the water relative permeability curve using the Brooks-Corey coefficients found by (Kapetas et al., 2017) for Berea rocks in Figure 19.

**Table 4:** Average water saturation and water relative permeability in sections of the core where degassing has occurred for all experiments

Section of core	$s_{CO_2}$ [mol/L]	$p_b$ [bar]	$\langle S_w \rangle$	$k_{rw}$
Last	0.3	1	0.717	0.146
Last	0.5	1	0.636	0.0824
Second to last	0.5	1	0.769	0.382
Last	0.7	3	0.643	0.102
Second to last	0.7	3	0.658	0.148
Last	0.9	10	0.657	0.0822
Second to last	0.9	10	0.675	0.102
Last	1.1	2	0.636	0.0874
Second to last	1.1	2	0.644	0.0947
Last	1.3	18	0.654	0.107
Second to last	1.3	18	0.666	0.117

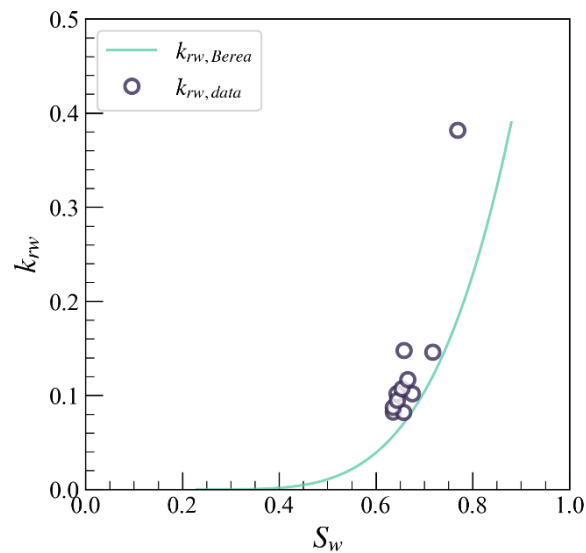


**Figure 19:** Brooks-Corey water relative permeability function along with experimental data

All of the experimentally determined relative permeability values are reasonably close to the predicted values, but the values are also consistently higher than the curve predicts. This can be due to sample variation of the core used here compared to that for the curve. The relative permeability values in the second to last section are higher than that in the last section for all experiments, which is caused by less free gas being present there. The abrupt decline due to degassing that has been observed in all experiments using the Berea sandstone means that the values of water saturation and relative permeability are also similar for of the performed experiments. The relative permeability values found here are all clustered around 0.1. The only exception here is the second to last section in the experiment using a  $\text{CO}_2$  concentration of 0.5 mol/L, because in that case the free gas had not spread through the entire section of the core thus not decreasing the relative permeability of the core so much. This is also the reason why the second to last section of the core was not taken into consideration for the experiment using 0.3 mol/L  $\text{CO}_2$  concentration as there was no free gas found in that section. The water saturation does not reduce below a value of about 0.63, but instead the degassing front moves upwards into the core at lower pressures. This explains why the permeability decrease observed in all the experiments (see e.g. Figure 11) quickly reaches a plateau and does not reduce further at lower pressures. This is believed to be dependent on the rock type that is used as previous experiments using a more permeable Bentheimer sandstone (Boeije et al., 2022b) showed a more gradual decrease in effective permeability.

#### 4.4 CONCLUSIONS AND RECOMMENDATIONS

- Using a higher salinity brine instead of tap water causes the degassing process to start at a higher pressure due to reduced CO<sub>2</sub> solubility with higher salinities leading to increased deviations. It does not change the degree to which the degassing process alters the effective permeability.
- In order to correctly predict the degassing behavior in the presence of saline brines, more advanced models are needed than the Van 't Hoff equation used for CO<sub>2</sub> solubility estimation in this study. Such models are available in literature and typically use different equations of state such as that of (Duan and Sun, 2003).
- The extent to which the effective permeability is reduced by the formation of free gas is only very slightly affected by temperature and salinity. By increasing the temperature, the total decrease in effective permeability due to degassing went from 91% to 89% at 30 and 70 °C respectively. For an increase in salinity the change in effective permeability was negligible.
- CT visualization of the degassing process showed that at low CO<sub>2</sub> concentrations a fairly stable free gas front forms that moves upstream into the core as the back pressure is lowered. This is not the case at higher concentrations, where the effects of gravity override are more pronounced. In terms of water relative permeability, a value of approximately 0.1 is found in most of the regions where degassing takes place. Along with this comes a fairly constant of average water saturation in these zones down to 0.63. Instead of lowering the water saturation further, the free gas front advances upstream into the core.
- CT assisted coreflood experiments using a vertically oriented core are recommended to allow for more direct comparison with the experiments outside the CT scanner and to prevent the effect of gravity override on the results.

---

## 5 CONCLUSION

REFLECT Task 2.2 has resulted in an improved understanding of the physical principles of the degassing process  $\text{CO}_2$  from high salinity fluids and its implications for flow in both bulk and porous media. Results presented in this report have been disseminated either through journal publication or presentations at conferences.

A coreflooding setup has been designed and constructed that can be used to study the degassing process in rock cores at elevated temperatures (up to  $90^\circ\text{C}$ ) and pressures up to 100 bar. The coreholder used to house the rock core is made from PEEK, which allows application of CT imaging to visualize the internals of the rock core during the experiments.

Depressurization experiments in a visual cell have led to the following conclusions for the degassing of  $\text{CO}_2$  from high salinity fluids in bulk. For a 1 M NaCl brine combined with a high, 0.50 mol/kgw,  $\text{CO}_2$  concentration, a good match is found in the bubble point when comparing experimental and modelling results for the investigated pressure and temperature conditions using either the Duan and Sun or volume translated SRK EoS model. However, at lower  $\text{CO}_2$  concentrations, more significant differences are found between the model and experiment. The higher salinity brine (1.5 M  $\text{CaCl}_2$  + 2 M NaCl) has approximately three times lower  $\text{CO}_2$  solubility compared to the 1 M NaCl brine. A good match is found for experiment and model for this brine using a  $\text{CO}_2$  concentration of 0.15 mol/kgw, although deviations between experiments and the model increase at higher temperatures. At higher  $\text{CO}_2$  concentrations, the degassing already starts in the supercritical regime. Supercritical bubbles are found to be much smaller and also form in much greater numbers at or near the bubble point pressure compared to gaseous bubbles. Further experiments at higher temperatures are required to validate the solubility behaviour that is predicted by the geochemical model.

In porous media, using a higher salinity brine instead of tap water causes the degassing process to start at a higher pressure due to reduced  $\text{CO}_2$  solubility with higher salinities leading to increased deviations. The extent to which the effective permeability is reduced by the formation of free gas is only very slightly affected salinity. CT visualization of the degassing process showed that at low  $\text{CO}_2$  concentrations a fairly stable free gas front forms that moves upstream into the core as the back pressure is lowered. This is not the case at higher concentrations, where the effects of gravity override are more pronounced. In terms of water relative permeability, a value of approximately 0.1 is found in most of the regions where degassing takes place. Along with this comes a fairly constant average water saturation in these zones down to 0.63. Instead of lowering the water saturation further, the free gas front advances upstream into the core.



---

## 6 LIST OF PUBLICATIONS

Boeije, C.S., Weinzierl, W., Zitha, P.L.J. and Pluymakers, A.H.M., “Degassing kinetics of high salinity geothermal fluids”, presented at EGU General Assembly 2022, Vienna, Austria, 23 – 27 May 2022

Boeije, C.S., Weinzierl, W., Zitha, P.L.J. and Pluymakers, A.H.M., “Degassing kinetics of high salinity geothermal fluids”, accepted for publication in European Geologist Journal, Special Issue: Geothermal Energy

## 7 REFERENCES

- Aminu, M.D., Nabavi, S.A. and Manovic, V., 2018, CO<sub>2</sub>-brine-rock interactions: The effect of impurities on grain size distribution and reservoir permeability. *International Journal of Greenhouse Gas Control*, 78: 168-176.
- Arnórsson, S., 1989, Deposition of calcium carbonate minerals from geothermal waters — theoretical considerations. *Geothermics*, 18: 33-39.
- Bear, J., 2013, *Dynamics of Fluids in Porous Media*. Dover Publications
- Blöcher, G., Reinsch, T., Henniges, J., Milsch, H., Regenspurg, S., Kummerow, J., Francke, H., Kranz, S., Saadat, A., Zimmermann, G. and Huenges, E., 2016, Hydraulic history and current state of the deep geothermal reservoir Groß Schönebeck. *Geothermics*, 63: 27-43.
- Boeije, C., Zitha, P. and Pluymakers, A., 2022a, High-speed imaging of degassing kinetics of CO<sub>2</sub>-water mixtures. *Physics of Fluids*, 34: 123307.
- Boeije, C.S., Verweij, C., Zitha, P.L.J. and Pluymakers, A.H.M., Year, CO<sub>2</sub> degassing of geothermal fluids during core-flood experiments. *European Geothermal Congress 2022*, Berlin, Germany, 17 – 21 October 2022
- Chandrasekharam, D. and Bundschuh, J., 2008, *Low-Enthalpy Geothermal Resources for Power Generation*. CRC Press, London
- Chiodini, G., Baldini, A., Barberi, F., Carapezza, M.L., Cardellini, C., Frondini, F., Granieri, D. and Ranaldi, M., 2007, Carbon dioxide degassing at Lateral caldera (Italy): Evidence of geothermal reservoir and evaluation of its potential energy. *Journal of Geophysical Research: Solid Earth*, 112: 17.
- Cosmo, R.d.P., Ressel Pereira, F.d.A., Ribeiro, D.d.C., Barros, W.Q. and Martins, A.L., 2019, Estimating CO<sub>2</sub> degassing effect on CaCO<sub>3</sub> precipitation under oil well conditions. *Journal of Petroleum Science and Engineering*, 181: 106207.
- De Lucia, M. and Kühn, M., 2021, Geochemical and reactive transport modelling in R with the RedModRphree package. *Advances in Geosciences*, 56: 33-43.
- Duan, Z. and Sun, R., 2003, An improved model calculating CO<sub>2</sub> solubility in pure water and aqueous NaCl solutions from 273 to 533 K and from 0 to 2000 bar. *Chemical Geology*, 193: 257-271.
- Flores, J., Meza, O., Moya, S.L. and Aragón, A., 2017, The effect of salinity and gas saturation of a geothermal fluid on the reservoir permeability reduction. *Geofísica Internacional*, 56: 335-343.

- Fronadini, F., Caliro, S., Cardellini, C., Chiodini, G. and Morgantini, N., 2009, Carbon dioxide degassing and thermal energy release in the Monte Amiata volcanic-geothermal area (Italy). *Applied Geochemistry*, 24: 860-875.
- Fu, Y., van Berk, W. and Schulz, H.-M., 2013, Temporal and spatial development of scale formation: One-dimensional hydrogeochemical transport modeling. *Journal of Petroleum Science and Engineering*, 112: 273-283.
- Haizlip, J., Stover, M., Garg, S., Tut Haklidir, F. and Prina, N., Year, Origin and Impacts of High Concentrations of Carbon Dioxide in Geothermal Fluids of Western Turkey. 41st Workshop on Geothermal Reservoir Engineering, Stanford University, Stanford, California, February 22-24, 2016
- Kapetas, L., Vincent Bonniieu, S., Farajzadeh, R., Eftekhari, A.A., Shafian, S.R.M., Bahrim, R.Z.K. and Rossen, W.R., 2017, Effect of permeability on foam-model parameters: An integrated approach from core-flood experiments through to foam diversion calculations. *Colloids and Surfaces A: Physicochemical and Engineering Aspects*, 530: 172-180.
- Lamy-Chappuis, B., Angus, D., Fisher, Q., Grattoni, C. and Yardley, B.W.D., 2014, Rapid porosity and permeability changes of calcareous sandstone due to CO<sub>2</sub>-enriched brine injection. *Geophysical Research Letters*, 41: 399-406.
- Le Guennec, Y., Privat, R. and Jaubert, J.-N., 2016, Development of the translated-consistent tc-PR and tc-RK cubic equations of state for a safe and accurate prediction of volumetric, energetic and saturation properties of pure compounds in the sub- and super-critical domains. *Fluid Phase Equilibria*, 429: 301-312.
- Mahabadi, N., Zheng, X., Yun, T.S., van Paassen, L. and Jang, J., 2018, Gas Bubble Migration and Trapping in Porous Media: Pore-Scale Simulation. *Journal of Geophysical Research: Solid Earth*, 123: 1060-1071.
- Parkhurst, D.L. and Appelo, C.A.J., 2013, Description of input and examples for PHREEQC version 3: a computer program for speciation, batch-reaction, one-dimensional transport, and inverse geochemical calculations, Report 6-A43, U.S. Geological Survey Techniques and Methods, Reston, VA, 519 p.
- Pátzay, G., Stáhl, G., Kármán, F.H. and Kálmán, E., 1998, Modeling of scale formation and corrosion from geothermal water. *Electrochimica Acta*, 43: 137-147.
- Peiffer, L., Carrasco-Núñez, G., Mazot, A., Villanueva-Estrada, R.E., Inguaggiato, C., Bernard Romero, R., Rocha Miller, R. and Hernández Rojas, J., 2018, Soil degassing at the Los Humeros geothermal field (Mexico). *Journal of Volcanology and Geothermal Research*, 356: 163-174.
- Peng, D.-Y. and Robinson, D.B., 1976, A New Two-Constant Equation of State. *Industrial & Engineering Chemistry Fundamentals*, 15: 59-64.
- Rangel-German, E., Akin, S. and Castanier, L., 1999, Multiphase-Flow Properties of Fractured Porous Media.
- Rodríguez, F., Pérez, N.M., Melián, G.V., Padrón, E., Hernández, P.A., Asensio-Ramos, M., Padilla, G.D., Barrancos, J. and D'Auria, L., 2021, Exploration of deep-seated geothermal reservoirs in the Canary Islands by means of soil CO<sub>2</sub> degassing surveys. *Renewable Energy*, 164: 1017-1028.
- Sander, R., 2015, Compilation of Henry's law constants (version 4.0) for water as solvent. *Atmos. Chem. Phys.*, 15: 4399-4981.
- Soave, G., 1972, Equilibrium constants from a modified Redlich-Kwong equation of state. *Chemical Engineering Science*, 27: 1197-1203.

- Spycher, N., Pruess, K. and Ennis-King, J., 2003, CO<sub>2</sub>-H<sub>2</sub>O mixtures in the geological sequestration of CO<sub>2</sub>. I. Assessment and calculation of mutual solubilities from 12 to 100°C and up to 600 bar. *Geochimica Et Cosmochimica Acta - GEOCHIM COSMOCHIM ACTA*, 67: 3015-3031.
- Stefánsson, A., Keller, N.S., Robin, J.G., Kaasalainen, H., Björnsdóttir, S., Pétursdóttir, S., Jóhannesson, H. and Hreggvidsson, G.Ó., 2016, Quantifying mixing, boiling, degassing, oxidation and reactivity of thermal waters at Vonarskard, Iceland. *Journal of Volcanology and Geothermal Research*, 309: 53-62.
- Tamburello, G., Pondrelli, S., Chiodini, G. and Rouwet, D., 2018, Global-scale control of extensional tectonics on CO<sub>2</sub> earth degassing. *Nature Communications*, 9: 4608.
- Zuo, L., Krevor, S., Falta, R.W. and Benson, S.M., 2012, An Experimental Study of CO<sub>2</sub> Exsolution and Relative Permeability Measurements During CO<sub>2</sub> Saturated Water Depressurization. *Transport in Porous Media*, 91: 459-478.
- Zuo, L. and Benson, S.M., 2014, CO<sub>2</sub> Exsolution – challenges and Opportunities in Subsurface Flow Management. *Energy Procedia*, 63: 5664-5670.